



Corrosion and Wear Studies of Cr₃C₂NiCr-HVOF Coatings Sprayed on AA7050 T7 Under Cooling

M. Magnani, P.H. Suegama, N. Espallargas, C.S. Fugivara, S. Dosta, J.M. Guilemany, and A.V. Benedetti

(Submitted September 10, 2008; in revised form January 9, 2009)

In this work, cermet coatings were prepared by high-velocity oxygen-fuel (HVOF) technique using a Diamalloy 3007 powder. The influence of the spray parameters on corrosion, friction, and abrasive wear resistance was studied. The samples were obtained using the standard conditions (253 L/min of oxygen and 375 L/min of compressed air), higher oxygen flux (341 L/min), and higher carrier gas flux (500 L/min). The coatings were characterized using scanning electron microscopy (SEM), and x-ray diffraction (XRD). X-ray diffraction and SEM studies showed well-bounded coating/substrate interface, pores, metallic matrix, chromium oxides, carbides, and carbides dissolution into the matrix. In comparison with the standard condition, the sample prepared using higher oxygen flux showed the highest carbide dissolution because of the high temperature achieved in the spray process. When the carrier gas flux was increased, the sample showed denser structure because of the higher particle velocity. The friction and abrasive wear resistance of the coatings were studied using rubber wheel and ball-on-disk tests. All samples showed similar sliding and abrasive behavior, and all of them showed better performance than the aluminum alloy. The electrochemical behavior was evaluated using open-circuit potential (E_{OC}) measurements, electrochemical impedance spectroscopy (EIS), and potentiodynamic polarization curves. The coating prepared with higher carrier gas flux showed the highest corrosion resistance in 3.5% NaCl solution and probably no pitting attack to the substrate occurred even after around 26 h of test. Tests performed for longer immersion times showed that the total impedance values significantly decreased (6 and 4 times) for samples sprayed using standard and higher oxygen flux, and no great change for sample sprayed using higher carrier gas flux was observed. The last sample presents a corrosion resistance around 200 times higher than the others.

Keywords aluminum alloy, corrosion, EIS, HVOF, spraying parameters, wear

1. Introduction

Aluminum alloys of 7xxx series (Al-Zn-Mg-Cu) have low hardness, poor tribological properties, and low corrosion resistance in aggressive medium, exhibit some resistance to stress-corrosion cracking, and, when in contact motion with other alloys, aluminum suffers from scoring, adhesive wear, plastic deformation, and severe metallic sliding and abrasion (Ref 1-4).

Different processes were used to increase the corrosion resistance of the aluminum alloy, maintaining or even

increasing the mechanical properties: heat treatments (Ref 5, 6), anodizing coatings (Ref 7, 8), deposition of metal-matrix composite by plasma transferred arc (Ref 9), physical vapor deposition (PVD) (Ref 10, 11), duplex treatment (Ref 12, 13), ion beam (Ref 14), hard chromium electroplating (Ref 15), and thermal spray processes (Ref 14, 16-21).

Among the thermal spray techniques, the high-velocity oxygen fuel (HVOF) is one of those used most often to replace hard chromium plating (Ref 22, 23), because coatings with low porosity, high density, excellent adhesive strength (Ref 23, 24), good tribological properties (Ref 20), and higher corrosion resistance when compared with other spraying technologies (Ref 25-27) can be produced. In the HVOF process, a suspension of powder in the carrier gas is injected into the combustion chamber of a gun, where a fuel (propylene, hydrogen, kerosene, etc.) is burnt with oxygen at high pressure, generating a spray with supersonic velocity (Ref 28, 29). Thermally sprayed coatings have emerged as an available solution for a wide range of wear-resistance applications to improve the service life of machine components (Ref 22).

There are many different powder materials that can be sprayed by HVOF process, such as ceramics, metal alloys, pure metals, cermets, and polymers (Ref 28-30). Cermet coatings, such as chromium carbide and tungsten-based

M. Magnani, P.H. Suegama, C.S. Fugivara, and A.V. Benedetti, Departamento Físico-Química, Instituto de Química, UNESP-Universidade Estadual Paulista, CP 355, 14801-970 Araraquara, SP, Brazil; and N. Espallargas, S. Dosta, and J.M. Guilemany, Departament de Ciència dels Materials i Enginyeria Metallúrgica, CPT Thermal Spray Centre, Materials Engineering, Universitat de Barcelona, C/Martí i Franquès 1, E-08028 Barcelona, Spain. Contact e-mail: marinamagnani@gmail.com.

carbide coatings are frequently used in gas and steam turbines and aeroengines to improve the resistance to sliding and abrasive and erosive wear (Ref 22). They can also usually increase the corrosion resistance of the substrate (Ref 16, 25, 26, 30, 31).

Different materials can be used as substrates for the HVOF technique such as: copper, steel, titanium, aluminum alloys, magnesium alloys, and so forth. There are only few studies that applied cermet materials on aluminum alloys (Ref 21), probably because it is difficult to obtain coatings of high hardness using standard conditions, which adheres on aluminum and aluminum alloy substrates, since the high residual stress generated during the thermal spray process can delaminate the coating/substrate (Ref 32, 33).

The temperature of aluminum and aluminum alloy substrates during the spray process is another very important factor that can contribute to the delaminating phenomenon, but its effect can be minimized applying different simultaneous cooling techniques and changing the spray parameters such as gas ratio and flow rate, spray distance, gun transverse speed, torch passes, and so forth (Ref 30, 31, 34).

The aim of this work is to study the influence of spray parameters (carrier gas velocity and the amount of oxygen flow) on wear and corrosion properties of Cr_3C_2 -NiCr coatings applied onto an AA 7050-T7 aluminum alloy using the HVOF technique. It is particularly important to note that the coatings were applied with simultaneous refrigeration of the substrate (Ref 35).

2. Experimental Procedure

An AA 7050-T7 aluminum alloy provided by Embraer (São José dos Campos, Brazil) with a nominal composition (wt.%) of 6.1 Zn, 2.2 Cu, 2.1 Mg, 0.05 Si, 0.08 Fe, 0.01 Mn, 0.11 Zr, 0.02 Ti, and a balance of Al was used as substrate. Similar compositions for AA 7050-T7 aluminum alloys were previously given in literature (Ref 36, 37). The T73 heat treatment was used in this work to increase the SCC resistance (Ref 5). Before the spraying process, rectangular ($100 \times 20 \times 5 \text{ mm}^3$) samples were degreased with acetone and grit blasted with white corundum, Al_2O_3 (grade 24) at 5.6 bar, 45° , and using a blasting distance of 250 mm, to get a surface with a mean roughness of around $5 \mu\text{m}$.

Cr_3C_2 -NiCr coatings were obtained using Sulzer Metco (Westbury, NY) Diamond Jet Hybrid DJH 2700 HVOF equipment (CPT-Universitat de Barcelona). The powder selected was a commercial $80\text{Cr}_3\text{C}_2$ -20NiCr (wt.%) Di-alloy 3007, where the NiCr matrix contained 80 wt.% Ni and 20 wt.% Cr. The thermal spray parameters are shown in Table 1. The coatings were thermally sprayed on

the aluminum alloy using three different parameters: (a) parameters supplied by the gun manufacturer (standard parameters), (b) higher temperature of the flame (greater amount of oxygen), and (c) higher particle velocity (greater flow of compressed air); this will also increase the temperature of the flame, but to a lesser degree compared to the parameter described in (b). All samples were cooled during the spraying process using a liquid nitrogen prototype device provided by Air Products (Air Products and Chemicals, Inc., Allentown, PA, USA) (Ref 35).

The microstructure of powder and coatings was studied using a JEOL 5310 scanning electron microscope (SEM, JEOL Ltd., Tokyo, Japan) coupled to an energy-dispersive analyzer (EDS), and the coating thickness was estimated from digital micrographs. The microhardness was obtained by cross-sectional measurements using a Vickers indenter with a load of 300 g (an average of 20 indentations per sample). The phase composition of the powder and coatings was studied using a Siemens D500 and D5000 x-ray generator (Siemens Corporation, Karlsruhe, Germany); $K\alpha$ (Cu) = 1.54 \AA radiation was used at 40 kV and 30 mA. The range recorded was 30 to 60° with step time of 0.05 s.

The abrasion tests for each coating were carried out using rubber-wheel equipment (ASTM G 65-91 D), with a rotating speed of 139 rpm, load of 50 N, and abrasive particles of SiO_2 (flow of $295 \pm 2 \text{ g/min}$). The wear rates were calculated by means of mass loss measurements.

The wear test was performed using ball-on-disk equipment, ASTM G 99-90. The test diameter was 16 mm, the counterpart was a bulk of WC-6Co ball, the normal load applied was 15 N, and the sample relative velocity was 131 rpm, with a total testing distance of 1000 m. The relative humidity was constant and lower than 20%, and tests were performed at room temperature. The wear tracks produced on the coatings were examined by SEM and a Zygo New View 100 Scanning White Light Interferometer (SWLI, Zygo Corporation, Middlefield, CT, USA), which works up to a depth of $100 \mu\text{m}$ with 0.1 nm resolution and 0.3 nm root mean square (rms) repeatability and lateral resolution of 500 nm.

The corrosion resistance of the coated aluminum alloys was evaluated by electrochemical impedance (EIS) measurements of the as-sprayed HVOF coated samples in 80 mL unstirred and aerated 3.5% NaCl solution. Open-circuit potential (E_{OC}) measurements were also performed in chloride solution. The potential was measured and referred to an $\text{Ag|AgCl|KCl}_{(\text{sat.})}$ electrode used as a reference and connected to the working solution through a Luggin capillary. A platinum network was used as an auxiliary electrode. Finally, a working electrode of each coated sample was placed at the lateral face of a

Table 1 Thermal spray parameters

Condition	Coating reference	Number of torches	Powder feed rate, g/min	C_3H_6 , L/min	Spraying distance, mm	O_2 , L/min	Air jet, L/min
1	D15S	15	38	77	250	253	375
2	D15H	15	38	77	250	341	375
3	D15F	15	38	77	250	253	>500

horizontal electrochemical cell, exposing a geometric area of 0.8 cm^2 to the solution. This area is generally different from the actual area exposed to the solution, since it depends on the electrolyte penetration, surface roughness, and on the many defects present in the cermet (Ref 31).

E_{OC} and EIS measurements were performed using a Potentiostat/Galvanostat E.G&G Parc-273 and a Frequency Response Analyzer Solartron-SI1255 (AMETEK, Inc., Paoli, PA, USA) coupled to a computer. The EIS tests were performed applying 10 mV (rms) to the E_{OC} value, starting from 5×10^4 to 10^{-2} Hz with 10 points/decade. For all samples, E_{OC} and EIS measurements were performed after 26 h in chloride-containing solution and at room temperature. Complementary experiments were also done after 72 h of immersion.

3. Results and Discussion

3.1 Structural Characterization

3.1.1 Cr_3C_2 -NiCr Powder. The XRD pattern for this powder (Fig. 1) shows the crystalline structure of the

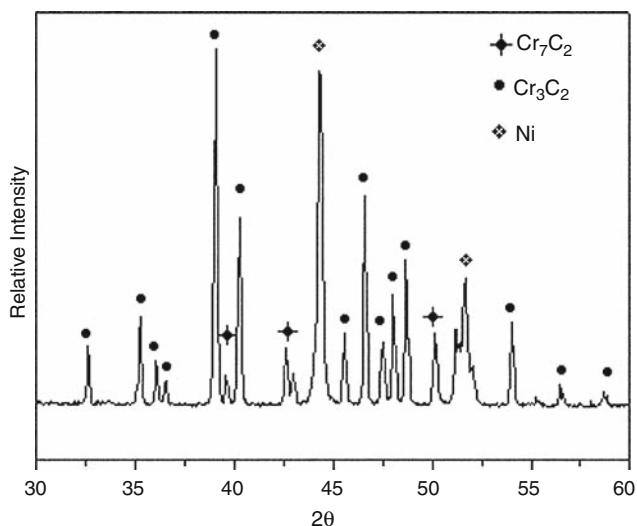
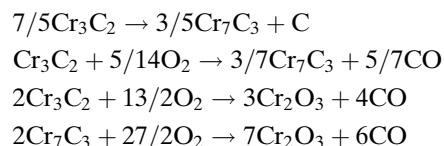


Fig. 1 XRD pattern for Cr_3C_2 -NiCr powder

material and the peaks are attributed to Cr_3C_2 , Cr_7C_3 , and Ni (solid solution of Cr in Ni) phases. Figure 2 shows that the powder presents a clad structure with carbide particles (size between 10 and $30 \mu\text{m}$) completely embedded in the nickel-chromium matrix. The particles show both faceted and rounded morphologies (Fig. 2), and the cross-section image clearly shows two phases with different contrasts (Fig. 2b): Ceramic phase (dark contrast) and metallic phase (light contrast).

3.1.2 Cr_3C_2 -NiCr Coating. X-ray diffraction analyses (Fig. 3) were carried out to identify the different phases present in the coatings, and patterns are different from the one obtained for the powder (Fig. 1). For all samples, chromium oxide and different carbide phases such as Cr_7C_3 and Cr_3C_2 were detected. Even though Cr_7C_3 carbide was already present in the initial powder, it was also produced by partial decomposition of the initial Cr_3C_2 phase during the spraying process (Ref 25). Chromium oxides were grown during the spraying process by a reaction of chromium with the oxygen that comes from the flame and also from the atmosphere. At high temperatures and oxidant atmosphere, several reactions can be involved in the decomposition of original phases and new phases formation (Ref 38):



The increase of the background intensity in the XRD spectra of the coatings is the main difference observed between the coatings and the feedstock material. This increase is caused by the formation of an amorphous noncrystalline phase (Ref 25), which in thermal spray processes appears mainly as a consequence of the very fast cooling of the coatings.

Scanning electron microscopic cross-section images (Fig. 4) of the coating/substrate interface showed well-bounded layers for all samples, sample D15S showed some delaminating in the coating (detail of Fig. 4a) but not in the coating/substrate interface (Fig. 4a).

Figure 5 shows SEM cross-section images (originals at $2000\times$) of the D15S (a), D15H (b), and D15F (c) coatings

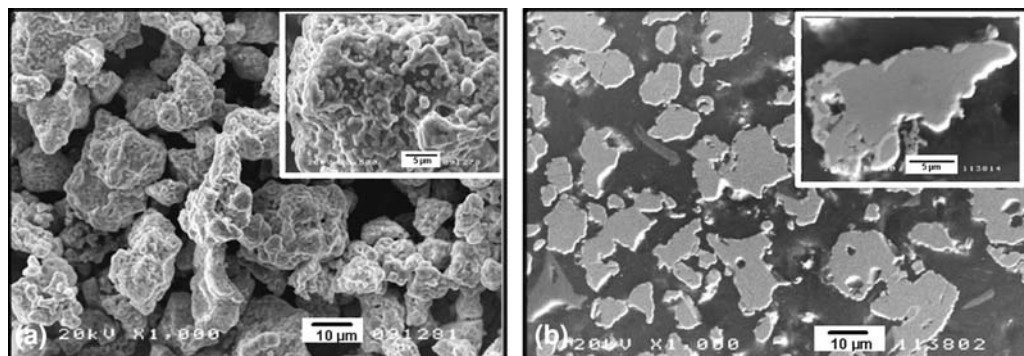


Fig. 2 SEM images of Cr_3C_2 -NiCr powder. (a) Three-dimensional section. (b) Cross section (inset: rough surface)

at high magnification. As a result of the spraying technique, all the coatings showed melted and semimelted particles of Cr_3C_2 in a NiCr matrix. The presence of (A) carbides, (B) melting zones, (C) pores, (D) oxides, and (E) matrix is observed, as previously described (Ref 25, 39).

The structure of sample D15H (Fig. 5b) shows a high number of oxidation-dissolution layers, as well as a high number of rounded Cr_3C_2 particles, as a result of the

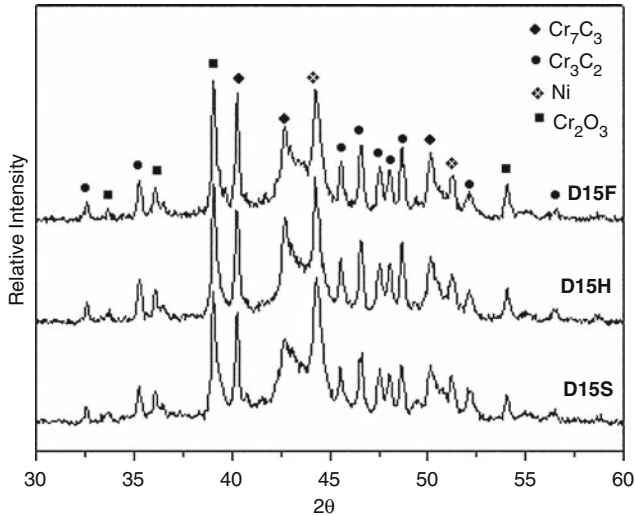


Fig. 3 XRD patterns obtained for samples D15H, D15F, and D15S

high temperature reached inside the flame during thermal spray process. Under these conditions, some carbide underwent superficial dissolution presenting a rounded form. The presence of low amount of oxidation-dissolution regions for samples D15F and D15S (Fig. 5a, c) was also observed. In the D15F sample, it is possible to observe the presence of more carbides and fewer oxidation-dissolution zones, indicating that the temperature was not enough high for dissolving the carbides probably because of the lesser exposition time to the flame.

The thicknesses of the coatings were around 210, 205, and 200 μm and the hardness was 960 ± 43 , 913 ± 37 , and 950 ± 39 HVN_{300} for samples D15S, D15H, and D15F, respectively, showing only a small difference in these parameters for the different coatings studied. The lowest hardness of D15H sample can be associated with the lower number of chromium carbides.

3.2 Tribological Properties

3.2.1 Sliding Wear Test (Ball-on-Disk). The evolution of the friction coefficient during the ball-on-disk test for all coatings are shown in Fig. 6, where it can be clearly seen that for the first 700 m of sliding, thermal spray coatings have higher friction coefficient than aluminum alloy. The mechanism that explains the sliding behavior of thermal spray coatings is the adhesion of the metallic binder to the counterpart followed by the pulling out of the carbides. The adhesion of the metallic phase promotes the increase of the friction coefficient, while the pullout of the ceramic phase generates a third body involved in

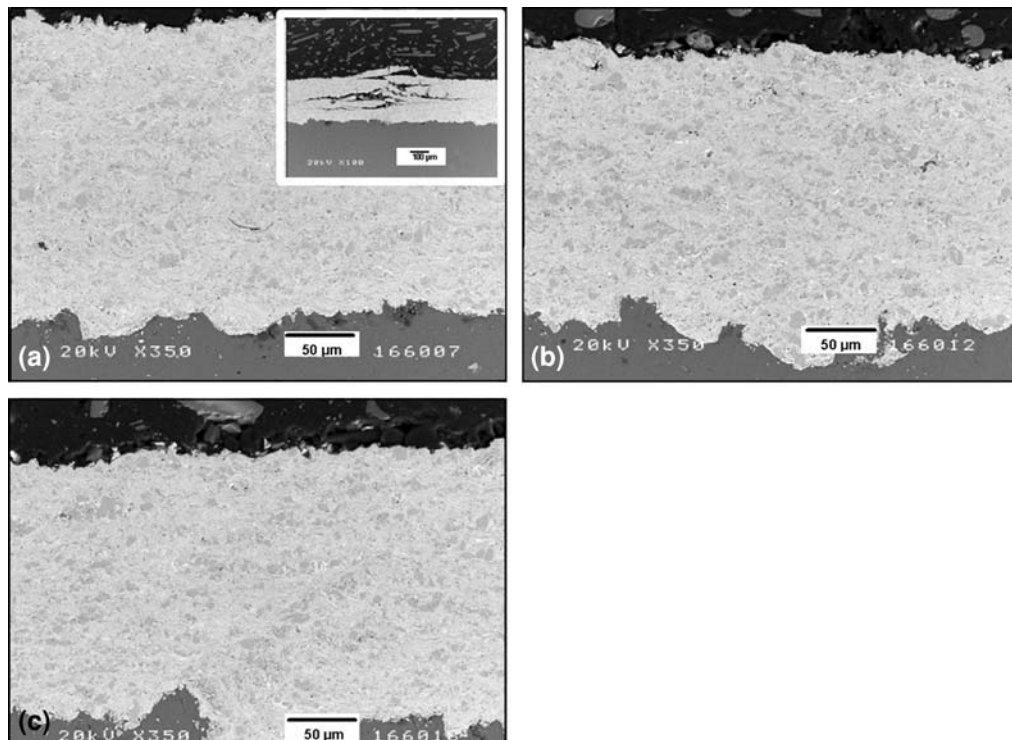


Fig. 4 SEM cross-section images of samples (a) D15S, (b) D15H, and (c) D15F

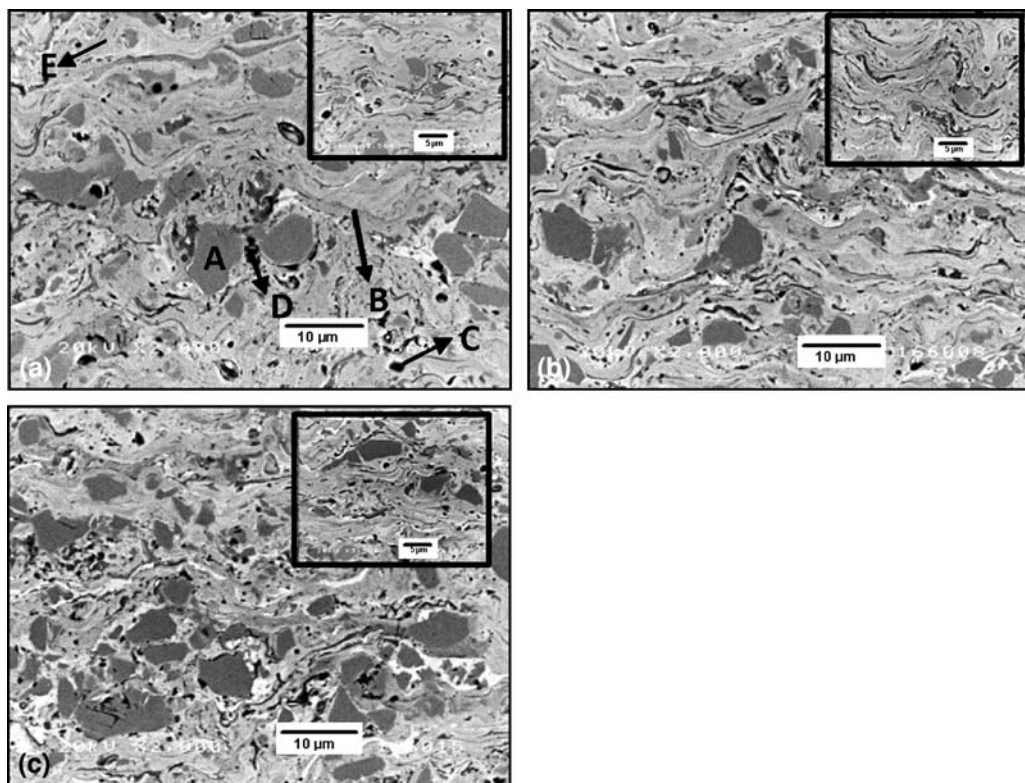


Fig. 5 SEM cross-section images of samples (a) D15S, (b) D15H, and (c) D15F

the sliding process that acts as an abrasive material. The abrasion generated during the friction test leads to an increase in the material loss. For the aluminum alloy sample, there are two different wear mechanisms involved. During the first 700 m of test, the high hardness of the counterpart (and also the normal load applied) produces plastic deformation in the aluminum surface, leading to a pulling out of material during sliding. This process produces debris that is pulled out during the sliding test, increasing the amount of material loss and decreasing the friction coefficient. After 700 m of test, the friction coefficient for the aluminum alloy increases up to the same value as observed for the coatings. It is well known that aluminum alloys are very sensitive to the temperature effect involved in the sliding process (Ref 38). Thus, for 700 m or more of test (a large number of cycles), the high temperatures achieved lead to an increase of the friction coefficient because of the transition from mild to severe wear, commonly observed in metals (Ref 38).

The SWLI profilometric images of the wear tracks are shown in Fig. 7. It can be clearly seen that the volume loss and material transferred from the counterpart is higher in the aluminum alloy than for samples with thermal spray coatings. When comparing all coatings, the lowest material loss was observed for sample D15F, which could be because of the presence of a great amount of unmelted powder particles in the coating.

After the sliding tests, SEM images of wear tracks show a high amount of material transferred between the

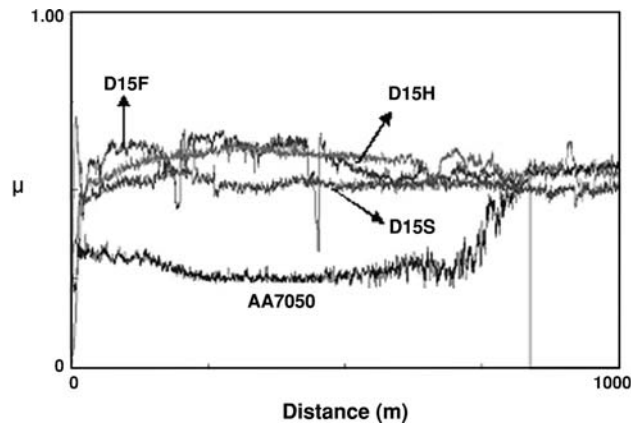


Fig. 6 Evolution of the friction coefficient for samples D15S, D15H, D15F, and AA70050 aluminum alloy

counterpart and the aluminum surface. An EDS analysis performed on a flake adhered on the wear track of sample D15S (Fig. 7d) showed peaks attributed to tungsten. For samples D15F and D15S, a high quantity of debris on the surface was observed. The debris are generated by the pulling out of the material (third body, which includes ceramic and metallic phases), and during the sliding process this material is deformed and remains stuck between the counterpart and the surface. So, particles with flaked shape on the surface of the wear track are formed as a

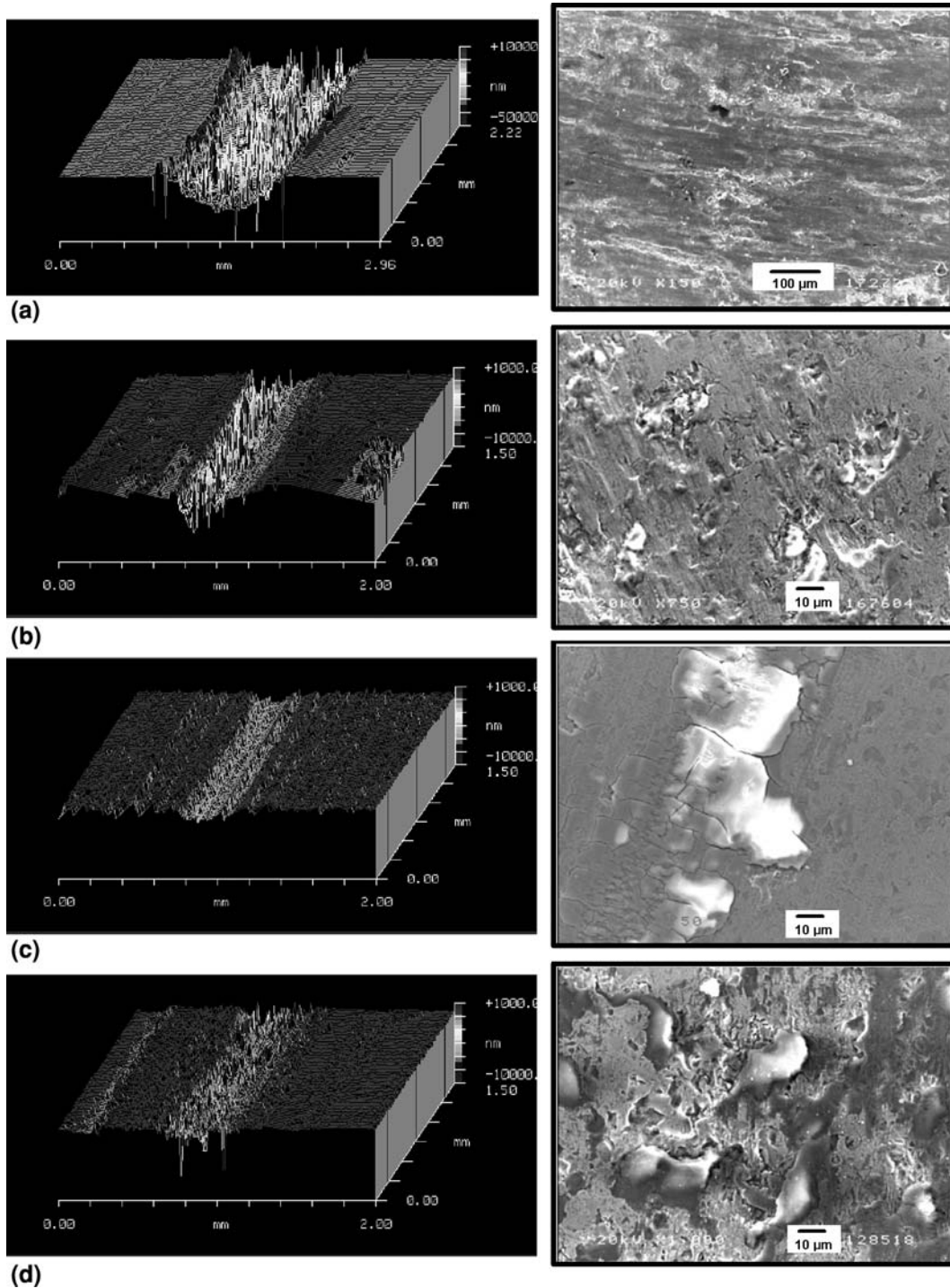


Fig. 7 SWLI and SEM images of the wear tracks after ball-on-disk tests for (a) AA7050-T7 aluminum alloy, (b) D15H, (c) D15F, and (d) D15S

consequence of this process (Fig. 7). However, the metallic phase is mainly responsible for the formation of the flakes on the surface of the wear track. Nevertheless, it seems that the amount of carbides removed from the matrix was lower for samples D15F and D15S than for sample D15H. This behavior could be due to: (a) at the

beginning of the test, the adhesion process in sample D15H takes place in a higher amount than for the other coatings and then, (b) when the abrasion mechanism begins it takes place in a larger amount than for samples D15F and D15S. The presence of a high amount of oxidation-dissolution areas in sample D15H could be

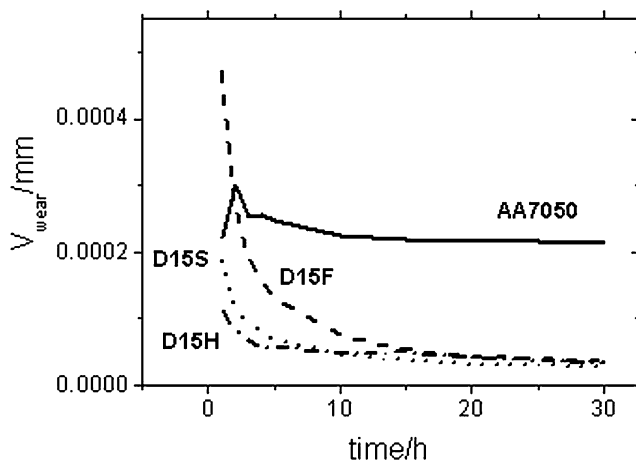


Fig. 8 Abrasive wear rate vs. time for samples D15S, D15H, and D15F, and AA7050-T7 aluminum alloy

responsible for its greater adhesion when compared with the other thermal spray coatings.

3.2.2 Abrasive Wear Test. Figure 8 shows the evolution of the abrasive wear rate versus time for all coatings and aluminum alloy. It can be observed that the wear rate of the same order of magnitude was measured for all coatings. Nevertheless, the aluminum alloy shows a wear rate about 10 times higher than that of thermal spray coatings. Therefore, it can be concluded that all coatings here obtained can offer good protection against abrasive wear for the AA7050-T7 aluminum alloy.

Rubber wheel tests were carried out without previous preparation of the samples surfaces. For shorter testing times, the decrease in the wear rate was higher for the thermal spray coatings than for the aluminum alloy due to the different initial surface roughness (R_a). This difference decreases until a steady state is achieved, and then the wear rate of the sample begins to stabilize. The measured wear rates were: $3.2 \times 10^{-5} \pm 3.4 \times 10^{-6}$; $4.5 \times 10^{-5} \pm 4.7 \times 10^{-6}$; $3.3 \times 10^{-5} \pm 2.3 \times 10^{-6}$; $2.1 \times 10^{-4} \pm 5.4 \times 10^{-5} \text{ mm}^3 \text{ N/m}$ for samples D15S, D15F, D15H, and aluminum alloy, respectively. These results indicated small differences in wear rate among thermal spray samples. Aluminum alloys are tougher than $\text{Cr}_3\text{C}_2\text{-NiCr}$ coatings, and their low hardness leads to a higher material loss during abrasion process.

3.3 Electrochemical Results

3.3.1 E_{OC} Measurements. Figure 9 shows the open-circuit potentials (E_{OC}) for samples D15S, D15H, and D15F and the AA7050-T7 aluminum alloy obtained in unstirred and aerated 3.5% NaCl solution during 24 h of immersion. For the AA7050-T7 aluminum alloy, the E_{OC} value increased from -0.69 to -0.62 V during the first 5 h of immersion and oscillated around this potential value until the end of the experiment. The E_{OC} values suggest that aluminum oxide is present on the alloy surface even before immersion, and it is modified in the chloride-containing solution by two processes occurring in the pits

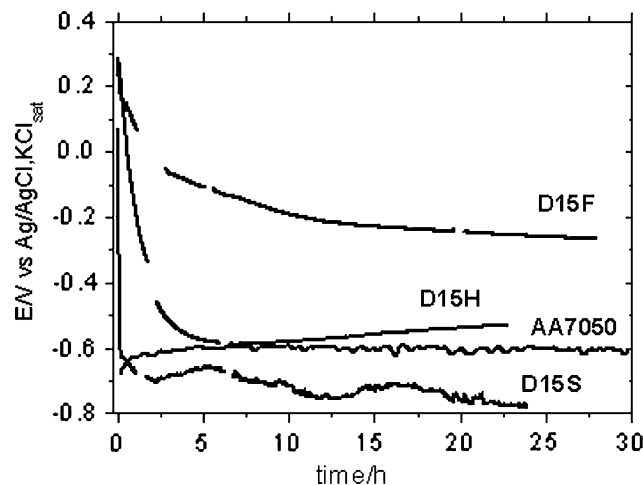
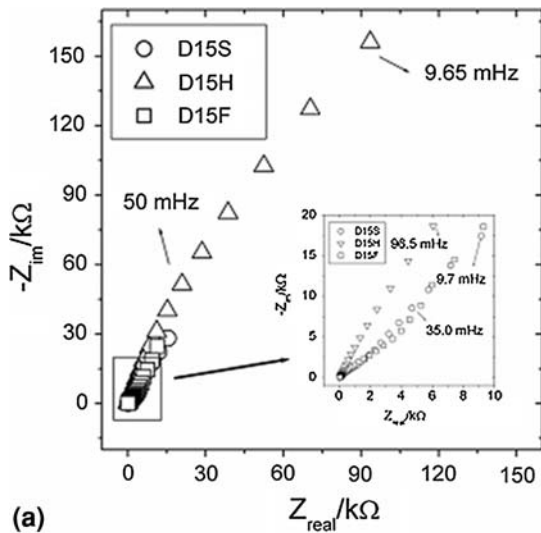


Fig. 9 Open-circuit potential (E_{OC}) vs. time curves for AA7050-T7 aluminum alloy and samples D15S, D15H, and D15F recorded in unstirred and aerated 3.5% NaCl solution

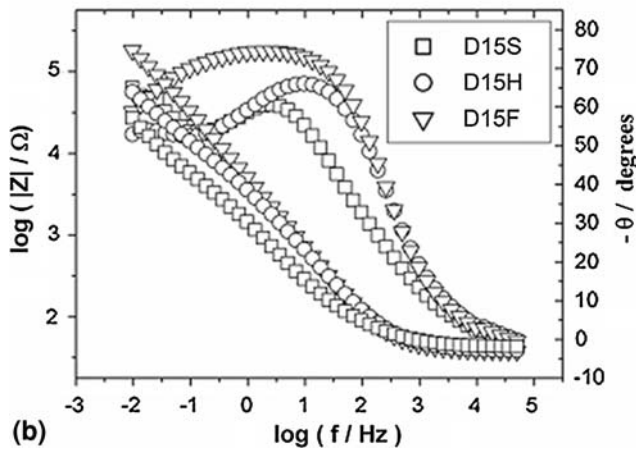
region: dissolution and repairing. These two phenomena are responsible for the potential oscillation.

For all coatings, the E_{OC} values decayed during the initial times of immersion stabilizing in -0.26 V (D15F), -0.52 V (D15H), and -0.78 V (D15S) after 24 h of immersion in 3.5% NaCl solution. The initial potential decaying is probably caused by the electrolyte penetration through the coating. The coating alone presented a less negative E_{OC} value (-0.18 V), and when the electrolyte reaches the Al substrate a galvanic pair is formed and the corrosion process at the coating/substrate interface can be accelerated. As a result the substrate is attacked and coating detachment can occur. Sample D15S showed the lowest E_{OC} value suggesting a rapid electrolyte penetration through the coating to reach the substrate. The oxide dissolution creating defects, pores and cracks facilitates the electrolyte penetration, and the corrosion of substrate is caused by the attack by chloride ions, leading to the formation of great amount of pitting corrosion products. The corrosion products can block the pores/cracks of the coating. However, for this sample it seems that oxide dissolution and some active sites are maintained in the regions where the electrolyte is in contact with the substrate. The final open-circuit potential measured is close to that for aluminum alloys in aerated chloride-containing solutions (Ref 40). Sample D15F showed the highest E_{OC} value, close to the one observed for the coating alone. It suggests a slow electrolyte penetration through the coating, delaying its contact with the substrate. This can be attributed to a denser and more homogeneous structure due to the high compressed air flow used during the thermal spray process, which produces a more compact coating. The D15H showed an intermediary behavior between samples D15F and D15S because of the lower impact velocity of the particles and higher temperature of the flame.

3.3.2 EIS Measurements. Figure 10 shows experimental Nyquist and Bode plots for all samples carried out after



(a)

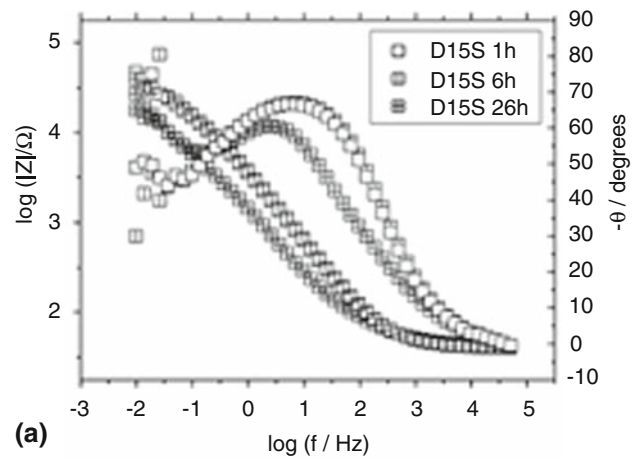


(b)

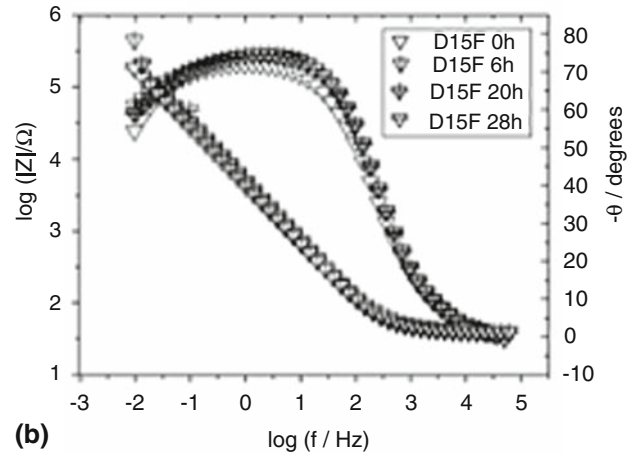
Fig. 10 Experimental (a) complex plane plots and (b) $\log |Z|$ and $-\phi$ vs. $\log (f)$ Bode plots for samples D15S, D15H, and D15F obtained in unstirred and aerated 3.5% NaCl solution after 26 h of immersion

26 h of immersion in chloride solution at open-circuit potential. The Nyquist plot (Fig. 10a) showed a capacitive semicircle that increases according to the following order: D15F \gg D15H $>$ D15S and the value of total impedance measured at 10 mHz was about 90, 34, and 11 k Ω for D15F, D15H, and D15S, respectively. These results are in good agreement with the tendency shown by E_{OC} values. Figures 10(b) and 11 show the evolution of Bode data with the immersion time and no changes in time constants and phase angle attributed to the coating response for samples D15H and D15F. Sample D15S shows a constant phase angle for 1 and 6 h of immersion at high frequency, which decreases with time (25 h) and shifts to lower frequency, followed by a dispersion of the data at low frequency. This is a clear indication that a coating degradation is in progress, suggesting that the contribution of the substrate to the global electrode process increased as the immersion time increased, probably because of the pit formation.

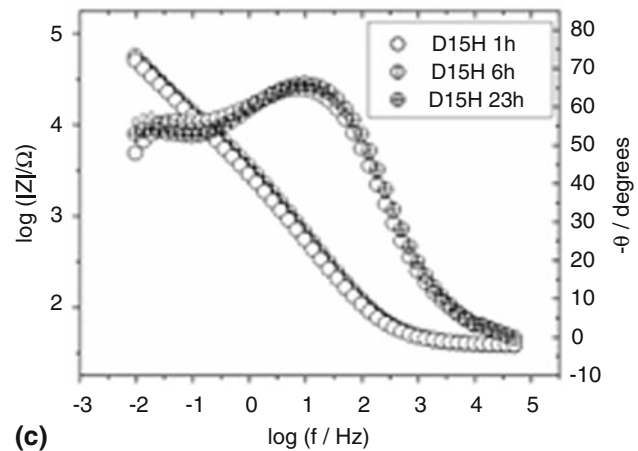
Sample D15F presented a time constant at higher frequencies (Fig. 10b and 11b), which was associated with the



(a)



(b)



(c)

Fig. 11 Experimental $\log |Z|$ and $-\phi$ vs. $\log (f)$ Bode plots for samples D15S (a), D15F (b), and D15H (c) for different immersion times at 25 $^{\circ}\text{C}$

response of the coating and embraces a large range (from almost 1 kHz to 1 Hz) of frequencies with a constant phase angle near 75 $^{\circ}$ throughout this frequency range, indicating a more capacitive behavior due to the compact structure of this coating. The higher compactness of this

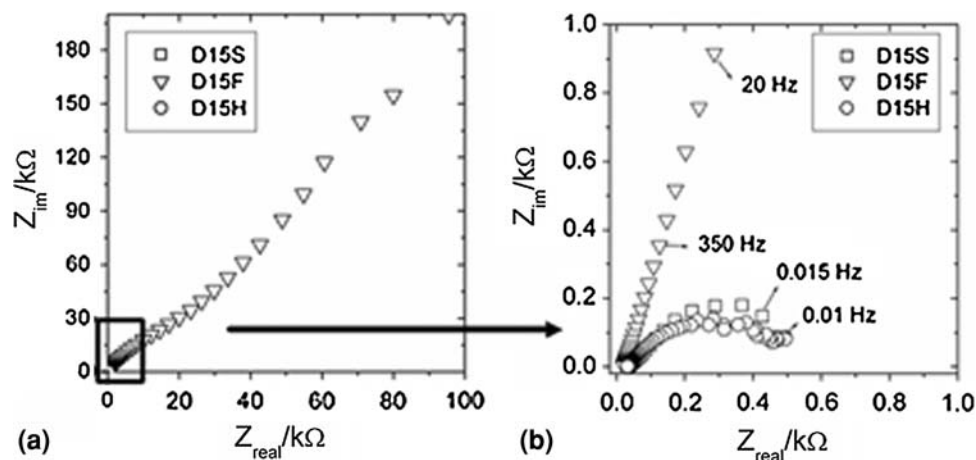


Fig. 12 (a) Experimental complex plane plots for samples D15S, D15F, and D15H for 72 h of immersion in NaCl solution and (b) zoom of the high frequency region

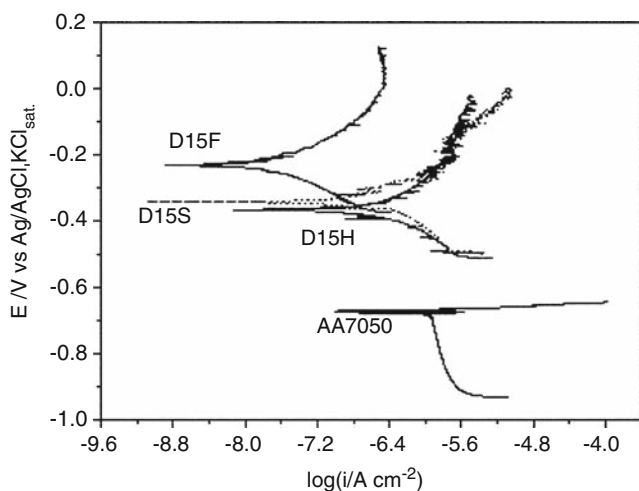


Fig. 13 Potentiodynamic polarization curves for D15S, D15F, D15H samples and aluminum alloy 7050 in unstirred and aerated 3.5% NaCl solution

coating likely prevents the corrosion of the substrate by pitting attack during the testing, and since both the substrate and coating corresponding time constants remain the same no coating degradation is evident. In the case of D15H, the phase angle remains constant with immersion time at high frequencies, while the one at low frequencies decreases, suggesting some modification on the substrate surface. For samples D15H and D15S, Bode phase plots (Fig. 10b and 11a, c) showed a well-defined time constant embracing around 10 Hz and centered at 10 and 2 Hz, respectively, with a phase angle from 65 to 70°. This time constant is related to the coating and aluminum oxides mainly for the D15S sample. For the D15H and D15S samples, another time constant seems to appear at low-frequency region with a maximum at 0.1 Hz, which is associated to the pitting process or corrosion of substrate.

The samples were also analyzed after 72 h of NaCl solution (Fig. 12). The following values for the total impedance were measured: 100 kΩ (D15F), 0.5 kΩ (D15H), 0.4 kΩ (D15S). It is clear that the total impedance values significantly decreased (6 and 4 times) with immersion time for samples D15H and D15S, while no great change for sample D15F was observed. Then, the thermal spray parameters have strong influence on the total resistance values of these samples, and the D15F sample presents a corrosion resistance around 200 times higher than the others.

3.3.3 Polarization Studies. Potentiodynamic polarization curves for all the coatings and aluminum 7050 alloy were recorded in aerated sodium chloride solution (Fig. 13). The estimated corrosion potential (V) values were: -0.22 (D15F) $>$ -0.33 (D15S) $>$ -0.37 (D15H) \gg -0.67 (AA7050 alloy), while the corrosion current ($i/\mu\text{A cm}^{-2}$) values were: 0.03 (D15F) $<$ 0.32 (D15S) $=$ 0.32 (D15H) \ll 1.1 (AA7050 alloy), indicating a corrosion potential difference of around 450 mV and 2 orders of magnitude in the current corrosion density between the best coating and the substrate. Therefore, the D15F sample showed the best performance among the coatings to protect the aluminum alloy substrate against corrosion in chloride solution, since it presented the most positive E_{corr} and the lowest corrosion current density value. Samples D15H and D15S showed similar E_{corr} and current density values, but their corrosion potential and corrosion current density were higher than aluminum alloy.

4. Conclusion

The present study clearly demonstrated the possibility of applying Cr_3C_2 -NiCr coatings on aluminum alloys without an intermediary metallic layer to minimize the effects of the very different thermal expansion coefficient between the coating and the aluminum alloy.

The structural characterization of the different coatings showed that samples prepared using higher oxygen or higher compressed air flux are well-bounded to the substrate, while the sample prepared using the standard conditions showed cracks with some delaminating inside the coating. The coating prepared using higher compressed air flux is denser than the others.

All studied coatings presented high sliding compared with the aluminum alloy, and the abrasive wear resistance was at least 10 times higher than for the AA7050-T7 aluminum alloy. The coating sprayed using higher carrier gas flux showed the highest corrosion resistance in 3.5% NaCl solution, and no pitting attack to the substrate occurred even after around 26 h of test.

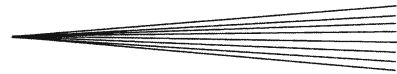
Tests performed for longer immersion times (72 h) showed that the total impedance values significantly decreased (6 and 4 times) for samples sprayed using standard and higher oxygen flux, and no great change for sample sprayed using higher carrier gas flux was observed. The last sample presents a corrosion resistance around 200 times higher than the others.

Acknowledgments

The authors wish to thank FAPESP (proc. n° 02/11542-4; 02/00448-7; 05/11542-4; 05/51851-4), CAPES (BEX-2283/04-2) and CNPq (proc.n° 300728/2007-7) for the scholarships, Generalitat de Catalunya for financial support (Project 2005SGR00310) and the CPT—Thermal Spray Centre, Universitat de Barcelona, Barcelona, Spain for samples preparation. The authors also wish to thank Air Products for the facilities to use the cooling device and Embraer (Empresa Brasileira de Aeronáutica S.A.) for providing the AA 7050 aluminum alloy samples.

References

1. Y. Sun, Tribological Rutile-TiO₂ Coating on Aluminium Alloy, *Appl. Surf. Sci.*, 2004, **233**(1-4), p 328-335
2. M.J. Ghazali, W.M. Rainforth, and H. Jones, The Wear of Wrought Aluminium Alloys under Dry Sliding Conditions, *Tribol. Int.*, 2007, **40**(2), p 160-169
3. P. Leo, E. Cerri, P.P. Marco, and H.J. Roven, Properties and Deformation Behaviour of Severe Plastic Deformed Aluminium Alloys, *J. Mater. Process. Technol.*, 2007, **2**(1-3), p 207-214
4. T. Yasmin, A.A. Khalid, and M.M. Haque, Tribological (Wear) Properties of Aluminum-Silicon Eutectic Base Alloy Under Dry Sliding Condition, *J. Mater. Process. Technol.*, 2004, **153-154**(10), p 833-838
5. J.C. Lin, H.-L. Liao, W.-D. Jehng, C.-H. Chang, and S.-L. Lee, Effect of Heat Treatments on the Tensile Strength and SCC-Resistance of AA7050 in an Alkaline Saline Solution, *Corros. Sci.*, 2006, **48**(10), p 3139-3156
6. L. Ceschini, I. Boromei, G. Minak, A. Morri, and F. Tarterini, Microstructure, Tensile and Fatigue Properties of AA6061/20 vol% Al₂O₃p friction stir welded joints, *Composites Part A: Appl. Sci. Manuf.*, 2007, **38**(4), p 1200-1210
7. R.G. Rateick, T.C. Binkowski, and B.C. Boray, Effects of Hard Anodize Thickness on the Fatigue of AA6061 and C355 Aluminium, *J. Mater. Sci. Lett.*, 1996, **15**(15), p 1321-1323
8. A. Merati and G. Eastaugh, Determination of Fatigue Related Discontinuity State of 7000 Series of Aerospace Aluminum Alloys, *Eng. Fail. Anal.*, 2007, **14**(4), p 673-685
9. R.L. Deuis, C. Subramanian, and J.M. Yellup, Abrasive Wear of Composite Coatings in a Salines and Slurry Environment, *Wear*, 1997, **203-204**, p 119-128
10. K. Kawata, H. Sugimura, and O. Takai, Characterization of Multilayer Films of Ti-Al-O-C-N System Prepared by Pulsed d.c. Plasma-Enhanced Chemical Vapor Deposition, *Thin Solid Films*, 2001, **390**(1-2), p 64-69
11. H. Hoche, C. Blawert, E. Broszeit, and C. Berger, Galvanic Corrosion Properties of Differently PVD-Treated Magnesium Die Cast Alloy AZ9, *Surf. Coat. Technol.*, 2005, **193**(1-3), p 223-229
12. M. Khaled, B.S. Yilbas, and J. Shirokoff, Electrochemical Study of Laser Nitrided and PVD TiN Coated Ti-6Al-4 V Alloy: The Observation of Selective Dissolution, *Surf. Coat. Technol.*, 2001, **148**(1), p 46-54
13. K.S. Klimek, H. Ahn, I. Seebach, M. Wang, and K.T. Rie, Duplex Process Applied for Die-Casting and Forging Tools, *Surf. Coat. Technol.*, 2003, **174-175**, p 677-680
14. J.V. Ringleben, Ch. Sundermann, T. Matsutani, M. Kiuchi, and W. Ensinger, Sealing Performance of Thin Amorphous Carbon Films Formed by Ion Beam Assisted Deposition at Low Temperature for Protection of Aluminium against Aggressive Media: The Influence of the Ion Energy, *Thin Solid Films*, 2005, **482**(1-2), p 115-119
15. A.L.M. Carvalho and H.J.C. Voorwald, Influence of Shot Peening and Hard Chromium Electroplating on the Fatigue Strength of 7050-T7451 Aluminum Alloy, *Int. J. Fat.*, 2007, **29**(7), p 1282-1291
16. M. Magnani, A.V. Benedetti, C.S. Fugivara, P.H. Suegama, and J.M. Guilemany, Analysis of Electrochemical Impedance and Noise Data for Thermal Spray Coatings in 3.5% NaCl Solution, *EUROCORR 2005* (Lisboa-Portugal), Anais do EUROCORR, 2005
17. S. Uozato, K. Nakata, and M. Ushio, Evaluation of Ferrous Powder Thermal Spray Coatings on Diesel Engine Cylinder Bores, *Surf. Coat. Technol.*, 2005, **200**(7), p 2580-2586
18. M.F. Morks, Y. Gao, N.F. Fahim, F.U. Yingqing, and M.A. Shoeib, Influence of Binder Materials on the Properties of Low Power Plasma Sprayed Cermet Coatings, *Surf. Coat. Technol.*, 2005, **199**(1), p 66-71
19. A. Edrisy, T. Perry, and A.T. Alpas, Investigation of Scuffing Damage in Aluminum Engines with Thermal Spray Coating, *Wear*, 2005, **259**(7-12), p 1056-1062
20. A. Edrisy, T. Perry, Y.T. Cheng, and A.T. Alpas, Wear of Thermal Spray Deposited Low Carbon Steel Coatings on Aluminum Alloys, *Wear*, 2004, **251**(1-12), p 1023-1033
21. P.M. Natishan, S.H. Lawrence, R.L. Foster, J. Lewis, and B.D. Sartwell, Salt Fog Corrosion Behavior of High-Velocity Oxygen-Fuel Thermal Spray Coatings Compared to Electrodeposited Hard Chromium, *Surf. Coat. Technol.*, 2000, **130**(2-3), p 218-223
22. J.K.N. Murthy and B. Venkataraman, Abrasive Wear Behaviour of WC-CoCr and Cr₃C₂-20(NiCr) Deposited by HVOF and Detonation Spray Processes, *Surf. Coat. Technol.*, 2006, **200**(8), p 2642-2652
23. M.P. Nascimento, R.C. Souza, I.M. Miguel, W.L. Pigatin, and H.J.C. Voorwald, Effects of Tungsten Carbide Thermal Spray Coating by HP/HVOF and Hard Chromium Electroplating on AISI 4340 High Strength Steel, *Surf. Coat. Technol.*, 2001, **138**(2-3), p 113-124
24. Y. Xie and H.M. Hawthorne, The Damage Mechanisms of Several Plasma-Sprayed Ceramic Coatings in Controlled Scratching, *Wear*, 1999, **233-235**, p 293-305
25. J.M. Guilemany, N. Espallargas, P.H. Suegama, and A.V. Benedetti, Comparative Study of Cr₃C₂-NiCr Coatings Obtained by HVOF and Hard Chromium Coatings, *Corros. Sci.*, 2006, **48**(10), p 2998-3013
26. P.H. Suegama, C.S. Fugivara, A.V. Benedetti, J. Fernández, J. Delgado, and J.M. Guilemany, Electrochemical Behaviour of Thermally Sprayed Cr₃C₂-NiCr Coatings in 0.5 m H₂SO₄ Environment, *J. Appl. Electrochem.*, 2002, **14**, p 1287-1295
27. J.M. Guilemany, C. Lorenzana, J. Nin, and J. Delgado, On-Line Monitoring Control of Stainless Steel Coatings Obtained by HVOF and APS Processes, *Proceedings of the United Thermal*



- Spray Congress and Exhibition (UTSC2002)* (Essen, Germany), 2002, p 86-90
28. L. Pawlowski, *The Science and Engineering of Thermal Spray Coatings*, John Wiley & Sons, New York, 1995
 29. V. Sobolev, J.M. Guilemany, and J. Nutting, *High Velocity Oxygen-Fuel Spraying*, Maney, England, 2004
 30. P.H. Suegama, C.S. Fugivara, A.V. Benedetti, J. Fernández, N. Espallargas, J. Delgado, and J.M. Guilemany, Microstructure and Electrochemical Studies of Cr₃C₂-NiCr Coatings, *New Researches on Electrochemistry*, E.P. Vargus, Ed., Nova Science Publishers, New York, 2007, p 113
 31. P.H. Suegama, N. Espallargas, J.M. Guilemany, J. Fernández, and A.V. Benedetti, Electrochemical and Structural Characterization of Treated Cr₃C₂-NiCr Coatings, *J. Electrochem. Soc.*, 2006, **153**, p B434-B445
 32. M. Magnani, P.H. Suegama, A.A.C. Recco, J.M. Guilemany, C.S. Fugivara, and A.V. Benedetti, WC-CoCr Coatings Sprayed by High Velocity Oxygen-Fuel (HVOF) Flame on AA7050 Aluminium Alloy: Electrochemical Behavior in 3.5% NaCl Solution, *Mater. Res.*, 2007, **10**(4), p 377-385
 33. J.A. Picas, A. Forn, R. Rilla, and E. Martín, HVOF Thermal Sprayed Coatings on Aluminium Alloys and Aluminium Matrix Composites, *Surf. Coat. Technol.*, 2005, **200**(1-4), p 1178-1181
 34. M. Wenzelburger, M. Escribano, and R. Gadow, Modeling of Thermally Sprayed Coatings on Light Metal Substrates: Layer Growth and Residual Stress Formation, *Surf. Coat. Technol.*, 2004, **180-181**, p 429-435
 35. M. Magnani, P.H. Suegama, N. Espallargas, S. Dosta, C.S. Fugivara, J.M. Guilemany, and A.V. Benedetti, Influence of HVOF Parameters on the Corrosion and Wear Resistance of WC-Co Coatings Sprayed on AA7050 T7, *Surf. Coat. Technol.*, 2008, **202**(19), p 4746-4757
 36. "Properties and Selection: Nonferrous Alloys and Special-Purpose Materials," *ASM Handbook*, Vol 2, 10th ed., ASM International, Materials Park, OH, 1992, p 1328
 37. J. Yan, L. Chunzhi, and Y. Minggao, On the η' Precipitate Phase in 7050 Aluminium Alloy, *Mater. Sci. Eng.*, 1991, **A141**, p 123-128
 38. M.I. Hutchings, *Tribology, Friction and Wear of Engineering Materials*, CRC Press, London, 1992, p 273
 39. P.H. Suegama, C.S. Fugivara, A.V. Benedetti, J.M. Guilemany, J. Fernández, and J. Delgado, The Influence of Gun Transverse Speed on Electrochemical Behaviour of Thermally Sprayed Cr₃C₂-NiCr Coatings in 0.5 M H₂SO₄ Solution, *Electrochim. Acta*, 2004, **49**, p 627-634
 40. P.L. Cabot, F. Centellas, J.A. Garrido, E. Perez, A.H. Moreira, P.T.A. Sumodjo, A.V. Benedetti, and W.G. Proud, Characterization of Localized Corrosion Processes in Al-Zn-Mg Alloys by Impedance Spectroscopy, *Progress in the Understanding and Prevention of Corrosion*, J.M. Costa and A.D. Mercer, Eds., Institute of Materials, London, **2**, 1993, p 1409-1418